Engineered Science
DOI: https://dx.doi.org/10.30919/es1608

Ultra-Broadband Flexible Absorber Utilising Multilayer Indium Tin Oxide Configurations

Zeng Qu,[1,2,*] Kangqiao Wang,[1] Qiuping Zhang,[4] Wenhua Zhang,[5] Yuanhao Huang,[1] Yibin Gong,[2,3] Haojian Wang,[2,3] Mengyuan Zhao,[1] Yuanhuui Wang,[1] Zhumao Lu,[6] Jiayun Wang[2,3] and Binzhen Zhang[2,3,*]

Abstract

This work demonstrates a metamaterial absorber with ultra-broadband flexible, utilizing a multi-layered indium tin oxide (ITO) configuration, accompanied by comprehensive simulations and fabrication processes. By employing a configuration incorporating periodic ITO-patterned layers printed on two polyethylene terephthalate (PET) dielectric substrates, the design achieves broadband absorption through enhanced Ohmic losses. Simulation analyses show that the designed structure maintains an absorption level of over 90% across a wide microwave spectrum ranging from 17.2 to 106.5 GHz. The fully symmetric architecture ensures polarization insensitivity, while maintaining excellent performance at incident angles up to 60°. The absorption mechanism is systematically investigated through impedance matching theory, complemented by analyses of surface current distributions and electric field patterns. An equivalent circuit model further elucidates the influence of structural parameters on absorption characteristics. Experimental validation via the arch reflectivity measurement method confirms strong agreement with simulation predictions. With outstanding advantages including ultra-broadband absorption, polarization independence, and mechanical flexibility, this absorber demonstrates significant potential for diverse applications such as electromagnetic imaging, sensing technologies, and stealth systems.

Keywords: Metamaterial absorber; Ultra-Broadband; Flexible; Electromagnetic waves.
Received: 23 May 2025; Revised: 28 June 2025; Accepted: 29 June 2025
Article type: Original research.

1. Introduction

Landy *et al.* first demonstrated the metamaterial perfect absorber (MPA) in 2008.[1] This classical design, featuring a sandwich structure composed of periodically arranged metallic patterned layers, dielectric spacers, and a flat metallic ground plane, has garnered significant attention due to its immense application potential in fields such as sensors,[2-6] energy harvesting,[7-9] modulators,[10] and spectral detection.[11] With subsequent improvements to the sandwich architecture, remarkable progress has been achieved in the design and investigation of metamaterial absorbers across diverse spectral regimes, spanning from microwave to visible light,[12-15] enabling absorption characteristics ranging from single-band to multi-band operation.[16-18] However, the inherently narrow absorption bandwidth of conventional metamaterial absorbers limits their applicability in broadband scenarios. Consequently, achieving broadband absorption holds critical importance for expanding their application scope.

Various strategies have been proposed to broaden the absorption bandwidth, such as integrating multiple resonators,[19,20] nested annular microstructures,[21] or incorporating lumped elements[22,23] within a single layer. However, these approaches suffer from two inherent limitations: bulky dimensions and relatively complex fabrication processes. In recent years, metamaterial absorbers based on indium tin oxide (ITO) resistive films have emerged as promising alternatives. Owing to their advantages including low cost, flexibility, commercial availability, optical transparency, and tunable electrical conductivity, ITO has been widely adopted as an exceptional material. Metamaterial absorbers utilizing ITO-patterned layers exhibit superior characteristics such as ultrathin profiles, enhanced optical performance, reduced weight, improved resolution, high transparency, and broader bandwidths. For instance, Jing Xu

[1]*School of Electrical and Control Engineering, North University of China, Taiyuan, 030051, China*
[2]*State Key Laboratory of Optoelectronic Dynamic Measurement Technology and Instrumentation for Extreme Environments, North University of China, Taiyuan, 030051, China*
[3]*School of Instrument and Electronics, North University of China, Taiyuan, 030051, China*

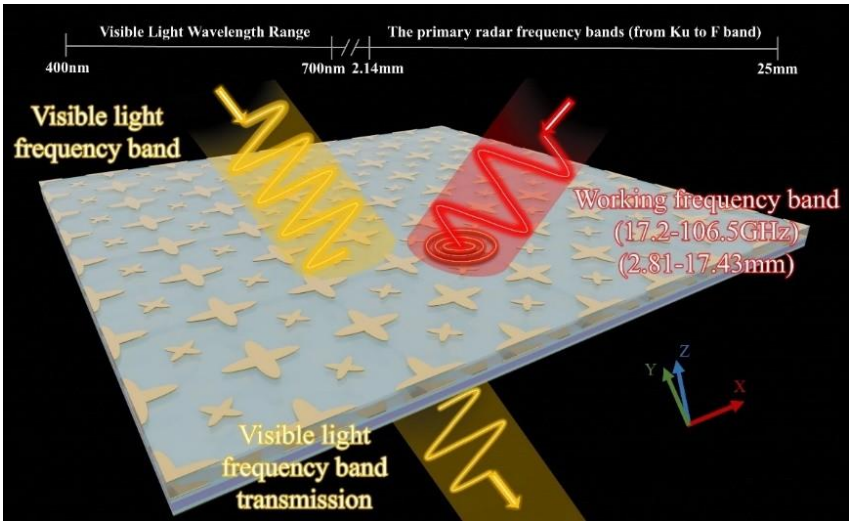

Fig. 1: Absorber hierarchical topology and performance specifications.

et al. developed a transparent microwave absorber metamaterial based on an ITO structure and low-loss glass substrate, achieving an absorption rate of over 90% in the 8-20 GHz frequency range and maintaining good performance over a wide incidence angle range of up to 60°.[24] Huihui Jing *et al.* demonstrated an ultra-wideband absorber utilising nested and stacked ITO resistive films, achieving over 90% absorption efficiency across the 19.68-94.7 GHz frequency range.[25] Yang Wang *et al.* proposed a reconfigurable transparent metamaterial absorber with a dual-layer ITO complementary resonant structure and a water-based substrate, operating in the 6.1-35.2 GHz frequency band with a relative bandwidth of up to 141%.[26] Senfeng Lai *et al.* designed a transparent ultra-wideband absorber for 5G communications, covering the 4-26 GHz operating frequency band.[27] Chang Yang *et al.* investigated a visible light and near-infrared transparent broadband microwave absorber based on silver nanowire (AgNW) films, achieving over 90% absorption efficiency in the 4.1-18.2 GHz frequency band and being insensitive to polarization.[28] Ahmet Teber proposed an ultra-thin, polarization-insensitive metamaterial absorber that exhibits excellent performance at a 15-degree oblique incidence angle, with an absorption rate exceeding 90% in the 24.30-28.12 GHz frequency band under normal incidence conditions.[29]

This work demonstrates a flexible metamaterial absorber with ultra-broadband flexible, utilizing a multi-layered indium tin oxide (ITO) configuration. Through optimized structural design, the absorber achieves over 90% electromagnetic wave absorption across an ultra-broad bandwidth of 17.2-106.5 GHz, corresponding to a relative absorption bandwidth of 144.4%. The designed architecture achieves polarization insensitivity while preserving broadband absorption stability across incidence angles up to 60°. A comprehensive analysis is conducted to investigate the influence of key parameters, including ITO thickness and surface resistance, on the performance of the patterned ITO films. By adjusting the number of ITO-patterned layers and integrating multiple ITO configurations, relevant parameters are optimized to significantly enhance absorption resonance effects. Compared to previous studies, the proposed architecture demonstrates notable advantages in ultra-broadband operation, wide-angle stability, and polarization-independent performance.

Table 1: Parameters of PET and PDMS.

	Dielectric constant	Loss tangent
PET	3.2	0.003
PDMS	2.35	0.06

Fig. 1 illustrates the layered topological configuration of the proposed absorber. The core structure comprises three functional layers: both the top and middle layers consist of periodic ITO resistive patterns fabricated on flexible polyethylene terephthalate (PET) substrates via precision etching. The middle layer is separated from the top layer by an air gap to establish electromagnetic coupling effects. The bottom layer integrates a PET film with a continuous ITO backplane, isolated from the middle layer by a polydimethylsiloxane (PDMS) spacer film. The material parameters of PET and PDMS are summarized in Table 1.

Fig. 2(a) illustrates the distinctive three-dimensional interlayer configuration of the absorber, with its structural parameters summarized in Table 2. The ITO patterns on the top and middle layers exhibit periodic planar distributions. The sheet resistances of the ITO films R_{Top}、R_{Middle} and R_{Bottom} are uniformly 50 Ω/sq.

2. Experimental

2.1 Simulation experiments

Conduct simulation experiments using CST Studio Suite 2023

[4]*Shanxi Normal University, Taiyuan, 030031, China*
[5]*School of Computer Science and Engineering, Nanjing University of Science and Technology, Nanjing, 210094, China*
[6]*State Grid Shanxi Electric Power Company Research Institute, 030001, China*
[*]*Email:* zqu@nuc.edu.cn (Zeng Qu), zhangbinzhen@nuc.edu.cn (Binzhen Zhang)

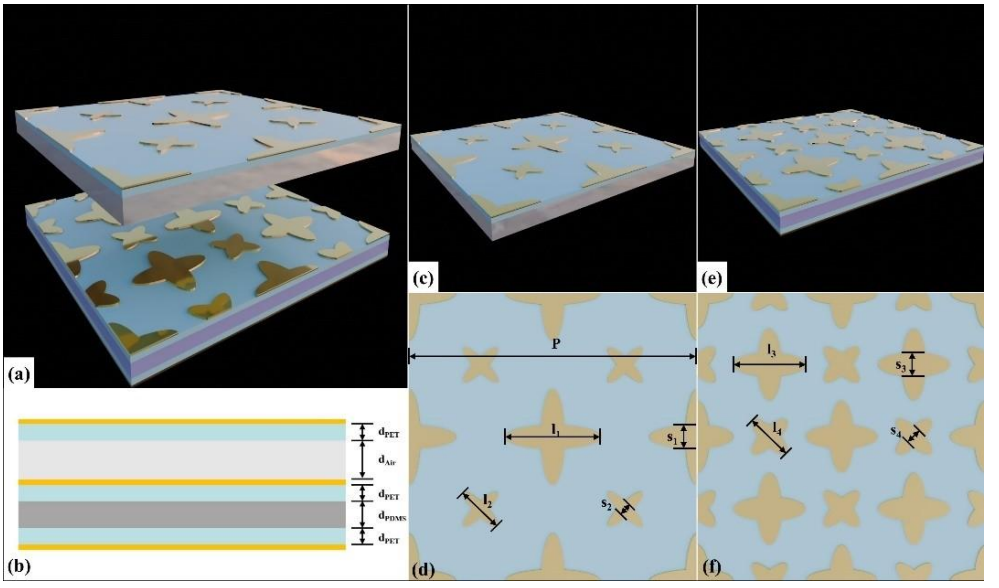

Fig. 2: (a) Unit cell breakdown, (b) Side-view profile, (c) Top-layer geometry with (d) top-view perspective, (e) Intermediate-layer geometry with (f) top-view configuration.

Table 2: Minimum unit structure size specification for metamaterials (Unit: mm) (λ_L denotes the maximum operating wavelength).

P	l_1	l_2	l_3	l_4	s_1	s_2	s_3	s_4	d_{PET}	d_{PDMS}	d_{Air}	Total thickness
12	2	1	1.5	1	0.5	0.25	0.5	0.35	0.175	0.4	0.6	1.525 ($0.0873\lambda_L$)

three-dimensional full-wave electromagnetic field simulation software. The simulation uses periodic boundaries (*x-y* plane) to represent structural periodicity, open boundary conditions (*z*-axis) to represent free space wave interactions, and TE-polarized excitation with the electric field vector parallel to the *y*-axis.

The absorption efficiency A(ω) was calculated using Eq. (1):

$$A(\omega) = 1 - R(\omega) - T(\omega) = 1 - |S_{11}(\omega)|^2 - |S_{21}(\omega)|^2 \quad (1)$$

In this equation, $R(\omega)$ and $T(\omega)$ are used to represent reflectance and transmittance, respectively. The S-parameters S_{11} and S_{21} are derived directly from the simulation.

Fig. 3 displays the simulated S-parameters and absorption spectrum. Due to the grounded ITO backplane acting as a reflective shield, the transmission parameter S_{21} remains negligible, simplifying Equation (1) to $A(\omega) = 1 - R(\omega)$. The absorber achieves over 90% absorption across an ultra-broad bandwidth of 17.2-106.5 GHz, corresponding to an absolute bandwidth of 89.3 GHz and a relative bandwidth of 144.4%. Notably, near-unity absorption (approaching 1) is observed at three distinct frequencies: 22.6 GHz, 62.5 GHz, and 91.1 GHz.

Fig. 4(a) illustrates the performance testing of the metamaterial absorber using the bow-tie reflectivity measurement method. The system consists of a bow-tie fixture, an antenna, the metamaterial test sample, a vector network analyzer, and the host equipment. The vector network analyzer is connected to the test sample via low-loss cables, and different frequency band antennas are used to accommodate the reflection testing of samples at various frequency bands. Fig. 4(b) and Fig. 4(c) show the top and middle layers of the ITO (indium tin oxide) array of the sample Fig. 4(d) and Fig. 4(e) demonstrate the transparency and flexibility of the sample.

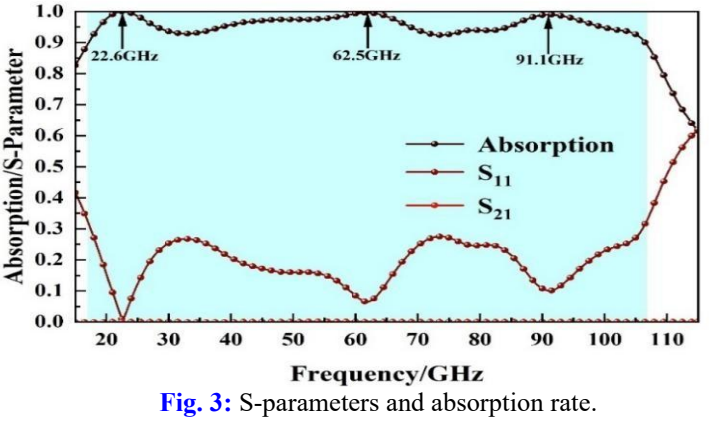

Fig. 3: S-parameters and absorption rate.

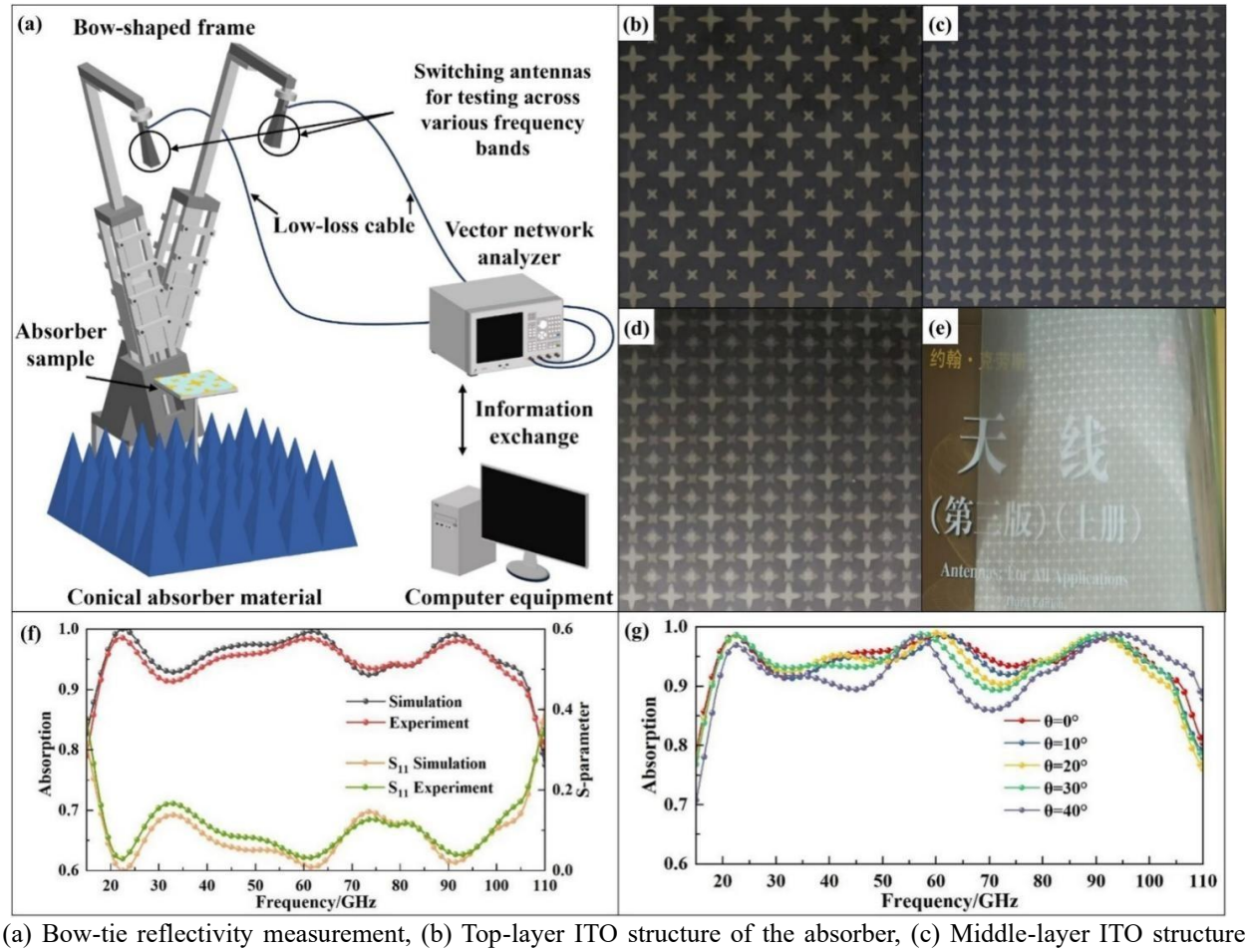

Fig. 4: (a) Bow-tie reflectivity measurement, (b) Top-layer ITO structure of the absorber, (c) Middle-layer ITO structure of the absorber, (d) Fabricated sample, (e) Flexibility of the sample, (f) Comparison of test and simulation results, (g) Oblique incidence test results.

Table 3: RLC Circuit parameters in the equivalent circuit.

Circuit parameters	Group					
	1	2	3	4	5	6
R(Ohm)	909	0.1	517	417	571	870
L(nH)	41.4	21.58	3.23	5.8	7.4	4.8
C(fF)	0.098	0.102016	0.83	10.48	0.825	2.45

Fig. 4(f)presents the comparison between the actual test results and the computer-simulated results under normal incidence conditions. Due to deviations in sample fabrication and the resistance of the resistive film from the ideal state, the actual results are slightly lower than the simulated results. Fig. 4(g) displays the measurement results at various incident angles, which still exhibit good performance and are in accordance with the simulated results.

3. Results and discussion

Absorption performance is determined by the S11, which depends mainly on the impedance matching between the absorber surface and free space. Theoretical analyses show that the electromagnetic energy dissipation is maximum when the two are optimally matched. To quantitatively evaluate impedance matching characteristics, the S-parameter inversion method can be employed to precisely derive the relative impedance of the material, as shown in Eq. (2):[30]

$$Z = \pm \sqrt{\frac{\left(1 + S_{11}(\omega)\right)^2 - S_{21}^2(\omega)}{\left(1 - S_{11}(\omega)\right)^2 - S_{21}^2(\omega)}} \quad (2)$$

The derived results of relative impedance Z(ω), effective permittivity ε(ω), and effective permeability μ(ω) are shown in Fig. 5.

The simulated results indicate that the real component of the absorber's relative impedance oscillates near unity, while its imaginary component maintains values approaching zero throughout the operational bandwidth. This demonstrates effective impedance alignment with free space, ensuring incident electromagnetic energy is efficiently channeled into the absorber's structure with minimal reflection. When the relative impedance's real part nears unity and its imaginary

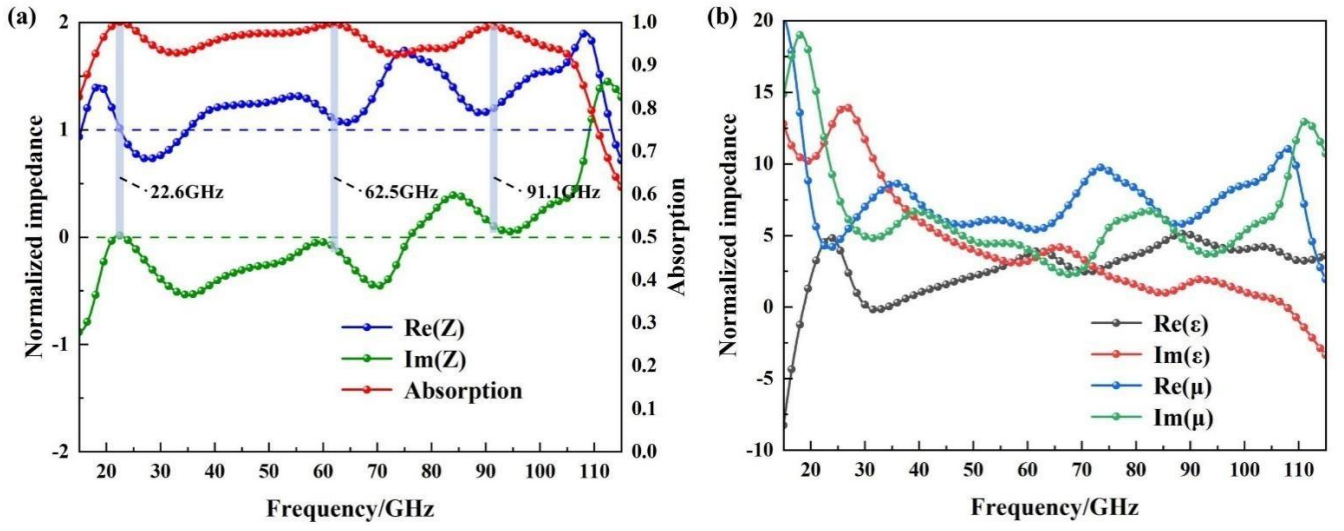

Fig. 5: Electromagnetic parameter analyses: (a) Absorbance versus relative impedance (Re[Z], Im[Z]) (b) Effective structural parameters (Re[ε/μ], Im[ε/μ]).

part approaches zero, surface reflection is markedly reduced, resulting in improved overall absorber performance. The convergence of the relative impedance to its ideal matching condition aligns the real and imaginary components of both effective permittivity and permeability in magnitude, enabling the theoretical absorption, as show in Eq: (3), to progressively approach the ideal 100% absorption limit.

$$A(\omega) = 1 - R(\omega) = 1 - \left|\frac{Z_{in} - Z_0}{Z_{in} - Z_0}\right|^2 \quad (3)$$

To better visualize the intrinsic absorption mechanisms, numerical simulations were conducted to comprehensively obtain electric field and surface current distributions at distinct absorption peaks. Fig. 6 depicts the electric field distributions of the top-layer and intermediate ITO patterns at three characteristic frequencies: 22.6, 62.5, and 91.1 GHz.

As shown in Figs. 6(a)-(b), at the 22.6 GHz resonant frequency, electric field energy concentration occurs predominantly at the tip regions of all cross-shaped units in the top-layer ITO etched structures, while the intermediate-layer ITO pattern exhibits localized field enhancement along the edge tips of its larger-scale cross structures. When the frequency increases to 62.5 GHz (Figs. 6(c)-(d)), the electric field intensity in large cross units of the top layer relatively attenuates, whereas significant enhancement emerges in small cross units. Concurrently, the intermediate layer demonstrates intensified overall field strength. At 91.1 GHz (Figs. 6(e)-(f)), the top-layer large cross structures exhibit substantial electric field intensification with conversely weakened small cross unit fields, while both large and small cross structures in the intermediate layer show diminished field strengths. This gradient electric field distribution characteristic across multi-scale structures reveals frequency-dependent coupling mechanisms of hierarchical resonant elements, ultimately achieving broadband absorption enhancement through

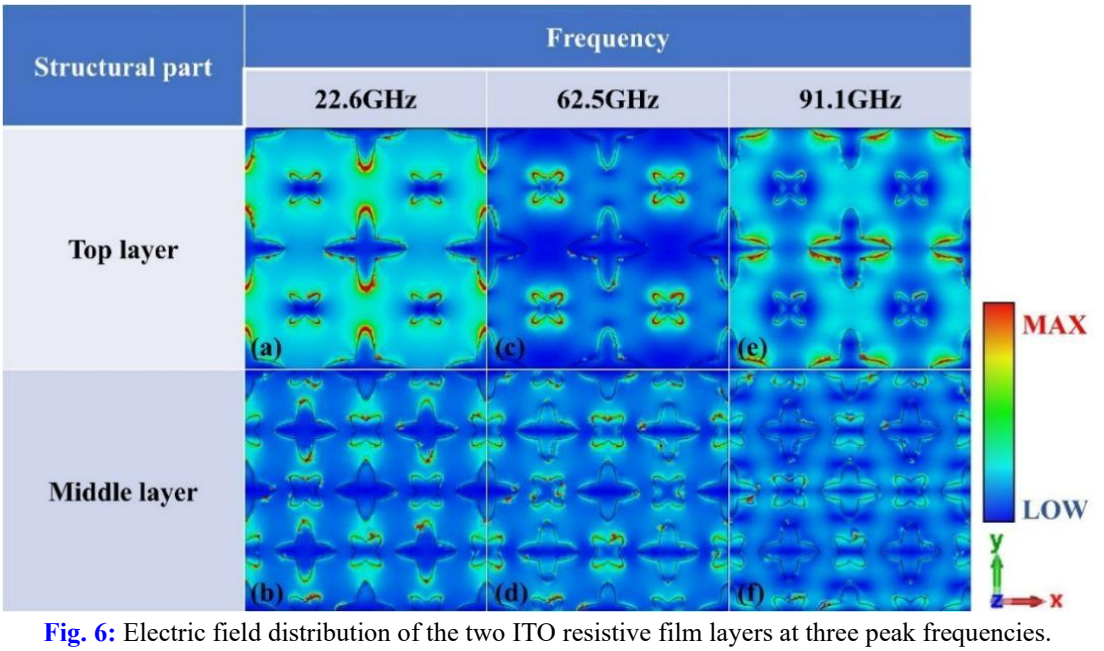

Fig. 6: Electric field distribution of the two ITO resistive film layers at three peak frequencies.

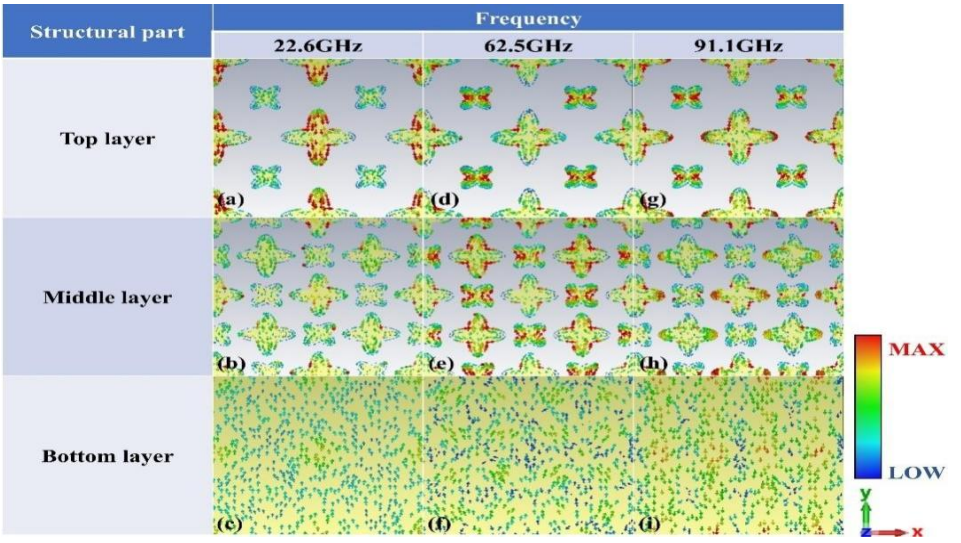

Fig. 7: Surface current distribution of the three ITO resistive film layers at three peak frequencies.

synergistic multi-modal resonances.

Fig. 7 simultaneously presents surface current responses of ITO conductive layers at three characteristic frequencies. Under 22.6 GHz resonance (Figs. 7(a)-(c)), surface currents predominantly concentrate on the top layer. Notably, the current flow directions in top and bottom layers exhibit antiparallel configurations, forming closed loops that effectively excite magnetic dipole resonances, thereby generating substantial electromagnetic energy dissipation.[31] At 62.5 GHz (Figs. 7(d)-(f)), enhanced surface currents emerge in both the intermediate-layer ITO structures and top-layer small cross units, collectively serving as the primary dielectric loss mechanism in this frequency range. For the 91.1 GHz high-frequency regime (Figs. 7(g)-(i)), strong current distributions in both top and intermediate layers induce considerable power loss, significantly contributing to absorption at 91.1 GHz. This confirms that broadband absorption can be achieved by strategically engineering spatial coupling configurations of ITO resistive patterns.

The regulatory effects of structural parameters including dielectric layer thickness and ITO surface resistance on absorption performance were systematically investigated. Fig. 8 illustrates the evolution of absorption characteristics under gradient variations of dielectric layer thickness. When d_{PDMS} is optimized from 0.8 mm to 0.4 mm, the effective bandwidth significantly widens. Thinning the dielectric layer promotes enhanced magnetic coupling effects between top and bottom structures, inducing a blue shift in resonant frequencies that directly strengthens the first absorption peak intensity. The second absorption peak primarily depends on the intermediate layer, showing minimal sensitivity to d_{PDMS} variations. The third absorption peak reveals synergistic effects in bilayer structures, where reduced interlayer distance intensifies bottom-layer coupling accompanied by frequency blue shifts, as demonstrated in Fig. 8(a).

Extending this parametric framework, the regulatory mechanism of d_{Air} on absorption performance was further elucidated. Given air's inherent impedance matching capability, the frequency response of the first absorption peak remains stable despite reduced d_{Air} induced top-bottom layer proximity. The second absorption peak exhibits moderate frequency shifts, while the third peak achieves bandwidth extension through blue-shifted resonance frequencies, as shown in Fig. 8(b). Optimizing both d_{PDMS} and d_{Air} enables the attainment of high absorption performance.

During structural parameter optimization, ITO surface resistance (Fig. 9) plays a critical role in absorption characteristics. Appropriate ITO surface resistance simultaneously enhances energy dissipation and maintains impedance matching conditions, thereby significantly improving overall absorption efficiency. The regulatory mechanisms of absorber structural parameters on performance can also be elucidated through equivalent circuit modeling. As shown in Fig. 10(a), the equivalent circuit analysis indicates

Table 4: Performance comparison of broadband absorbers.

Absorber	Thickness(mm)/λ_L	More than 90% absorption band width(GHz)	Fractional Band-width	Pattern layer	Polarization insensitivity	Flexible
Reference[24]	5/0.13λ_L	8-20	85.7%	1	Yes	Yes
Reference[25]	1.525/0.1λ_L	19.68-94.7	131%	2	Yes	Yes
Reference[26]	6.5/0.8883λ_L	4.1-18.2	127.1%	2	Yes	Yes
Reference[27]	2/0.0981λ_L	14.72-65.41	126.5%	2	Yes	Yes
Reference[28]	0.8/0.0867λ_L	32.5-42.5	26%	2	Yes	No
Reference[29]	1.670.1336λ_L	24-28.5	15.59%	1	Yes	No
This work	1.525/0.0874λ_L	17.2-106.5	144%	2	Yes	Yes

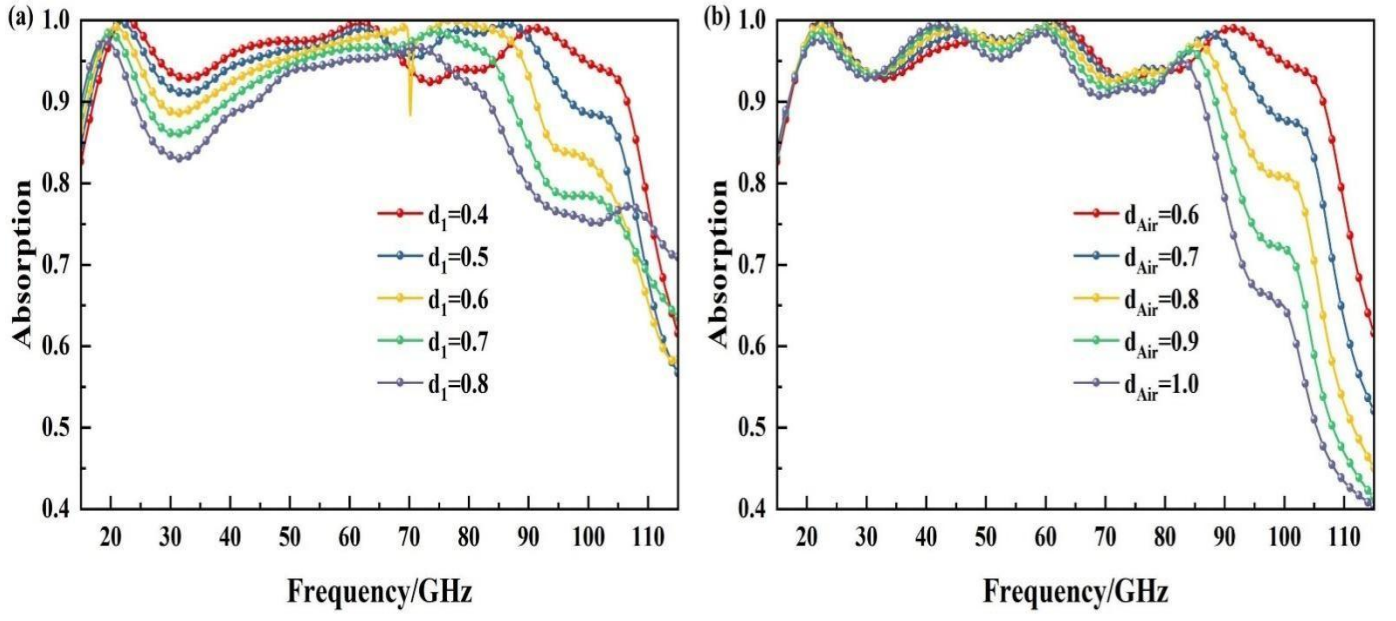

Fig. 8: Absorption properties under (a) PDMS and (b) Air with thickness gradient distribution.

that the energy dissipation mechanism is primarily controlled by RLC resonant elements. Since a single RLC series resonant structure is only suitable for single-frequency and narrowband absorption, the ADS simulation adopted a multi-channel RLC series resonant structure equivalent.[32] The first and second RLC series resonant structures approximately represent the equivalent losses of the two ITO patterns in the intermediate layer; the third to sixth RLC series resonant structures approximately represent the equivalent losses of the two ITO patterns in the top layer. A lossless transmission line ($Z_0 = 377\ \Omega$) is used to simulate free-space impedance matching conditions, which is critical for minimizing wave reflection. Within the equivalent circuit model framework, the bottom ITO ground plane is considered a short circuit ($Z \to 0$).

The mathematical expression for the energy dissipative RLC resonator is expressed as follows:

$$Z_{RLCi} = R_i + j\left(\omega L - \frac{1}{\omega C}\right), i = 1,2,\cdots,6 \tag{4}$$

Different dielectric materials can be characterized by their respective characteristic impedances:

$$Z_{PET} = \frac{Z_0}{\sqrt{\varepsilon_{PET}}}, Z_{Air} = \frac{Z_0}{\sqrt{\varepsilon_{Air}}}, Z_{PDMS} = \frac{Z_0}{\sqrt{\varepsilon_{PDMS}}} \tag{5}$$

In this equation, the relative permittivity of PET, air, and PDMS is denoted by $\varepsilon_{PET}, \varepsilon_{Air}$ and ε_{PDMS}, respectively.

The input impedance for each section can be derived as:

$$Z_a = \frac{jZ_0}{\sqrt{\varepsilon_{PET}}\tan(\beta_{PET}d_{PET})} \tag{6}$$

$$Z_b = Z_{Air}\frac{Z_a cos(\beta_{PDMS}d_{PDMS}) + jZ_{Air}sin(\beta_{PDMS}d_{PDMS})}{jZ_a sin(\beta_{PDMS}d_{PDMS}) + Z_{Air}cos(\beta_{PDMS}d_{PDMS})} \tag{7}$$

$$Z_c = Z_{PET}\frac{Z_b cos(\beta_{PET}d_{PET}) + jZ_{PET}sin(\beta_{PET}d_{PET})}{jZ_b sin(\beta_{PET}d_{PET}) + Z_{PET}cos(\beta_{PET}d_{PET})} \tag{8}$$

$$\frac{1}{Z_d} = \frac{1}{Z_{RLC1}} + \frac{1}{Z_{RLC2}} + \frac{1}{Z_c} \tag{9}$$

$$Z_e = Z_{PDMS}\frac{Z_d cos(\beta_{Air}d_{Air}) + jZ_{PET}sin(\beta_{Air}d_{Air})}{jZ_d sin(\beta_{Air}d_{Air}) + Z_{PET}cos(\beta_{Air}d_{Air})} \tag{10}$$

$$Z_f = Z_{PET}\frac{Z_e cos(\beta_{PET}d_{PET}) + jZ_{PET}sin(\beta_{PET}d_{PET})}{jZ_e sin(\beta_{PET}d_{PET}) + Z_{PET}cos(\beta_{PET}d_{PET})} \tag{11}$$

$$\frac{1}{Z_{in}} = \frac{1}{Z_{RLC3}} + \frac{1}{Z_{RLC4}} + \frac{1}{Z_{RLC5}} + \frac{1}{Z_{RLC6}} + \frac{1}{Z_f} \tag{12}$$

where β_{PET}, β_{Air} and β_{PDMS} represent the electromagnetic wave propagation constants in PET, Air, and PDMS, respectively.

The influence of incident direction and polarization states on electromagnetic wave absorption characteristics was systematically investigated. Fig. 11(a) demonstrates angular dependence under transverse electric (TE) polarization: Benefiting from the symmetrical structural design and multi-layer resonant coupling mechanisms, the broadband absorption profile maintains high stability even when the incidence angle increases to 60°.[33] Notably, beyond critical incidence angles, the low-frequency absorption efficiency exhibits significant attenuation. For transverse magnetic (TM) polarization scenarios (Fig. 11(b)), the absorber architecture similarly demonstrates exceptional wide-angle absorption capabilities, sustaining broadband performance up to 60° incidence. At extreme angles, high-frequency absorption displays compensatory enhancement, thereby balancing low-frequency performance degradation. Fig. 11(c) further reveals polarization-insensitive characteristics: As wave polarization rotates continuously from TE-aligned 0° to TM-aligned 90°,

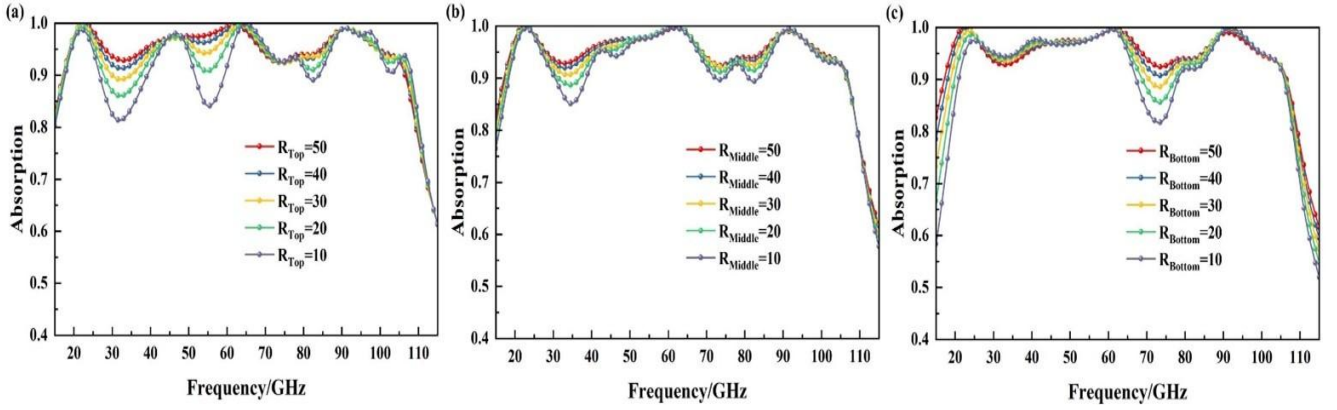

Fig. 9: Absorption performance under (a) R_{Top}, (b) R_{Middle} and (c) R_{Bottom} with gradient distribution.

the absorption spectrum remains stable due to the structure's geometric symmetry. At the same time, since the metamaterial absorber is dominated by the ohmic loss of the ITO layer, by optimizing the structural parameters as described above, the ohmic loss exhibits weak dependence on the incident angle. Therefore, within a certain range of incident angles, the absorption characteristics of the ITO layer remain relatively stable. Even when the incident angle changes, the ITO layer can still effectively dissipate electromagnetic energy, thereby achieving angle-insensitive absorption characteristics. These experimental results collectively confirm the successful co-optimization of ultra-broadband absorption and full-polarization compatibility in the proposed absorber configuration.

As shown in Fig. 12, the gradient expansion of absorption bandwidth is achieved through stacked multilayer ITO structures. By deconstructing and analyzing the independent absorption characteristics of individual components, the operational mechanism of the composite structure is revealed: Configuring gradient resonant unit arrays in the intermediate dielectric layer (Structure I→II, Figs. 12(a)-(b)) effectively excites coupled resonances across multiple frequency bands; Embedding heterogeneous ITO resonator stacks in multilayer dielectric substrates (Structure II→III, Figs. 12(b)-(c)) enables absorption band fusion through geometric dispersion control; Constructing multi-scale resonant units at the top layer (Structure III→IV, Figs. 12(c)-(d)) enhances interlayer electromagnetic coupling effects while introducing new resonance modes, ultimately forming a continuous broadband absorption response.

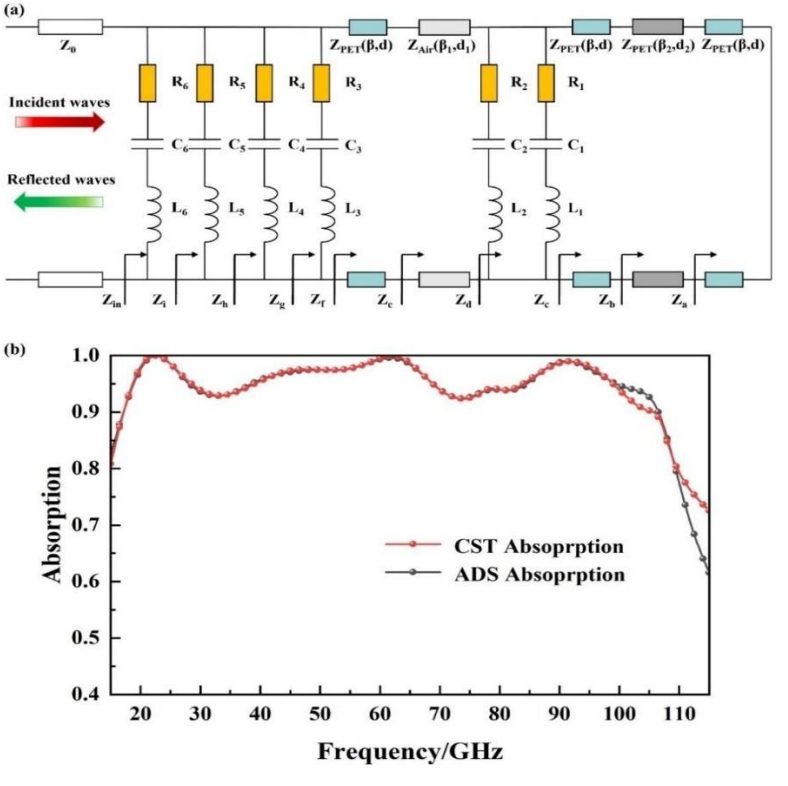

Fig. 10: (a) Equivalent circuit model (b) Comparison of ADS and CST simulations

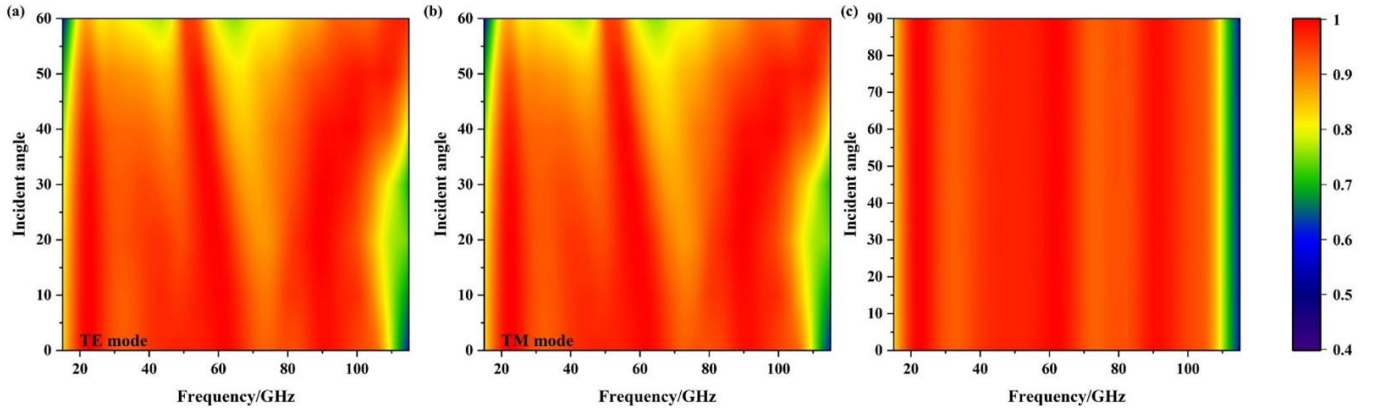

Fig. 11: Absorption performance of different (a) TE-polarized incidence angles, (b) TM-polarized incidence angles, (c) polarization angles.

As compared with existing results in Table 4. The meta mater ial absorber developed in this study demonstrates outstanding performance in terms of absorption bandwidth and relative bandwidth. Its absorption frequency range spans 17.2-106.5 GHz, with a relative bandwidth of 144%, both of which significantly exceed the results of other comparative studies. In terms of thickness, the absorber developed in this study has a thickness of 1.525 mm, with a wavelength-normalize thickness of 0.0874λ_L. Although not the thinnest, it is very close to New2 (0.8 mm/0.0867λ_L). A smaller wavelength-normalized thickness indicates that the absorber is thinner rel ative to its operating wavelength, meaning the designed absor ber is morelightweight and flexible, suitable for applications with weightand space constraints. The dual-layer structure de sign is maintained, which balances absorption performance with structural compactness to some extent. The absorber developed in this study also exhibits polarization insensitivity and flexibility, consistent with most comparative results, but achieves a more optimal balance in absorption performance, making it more competitive in practical applications.

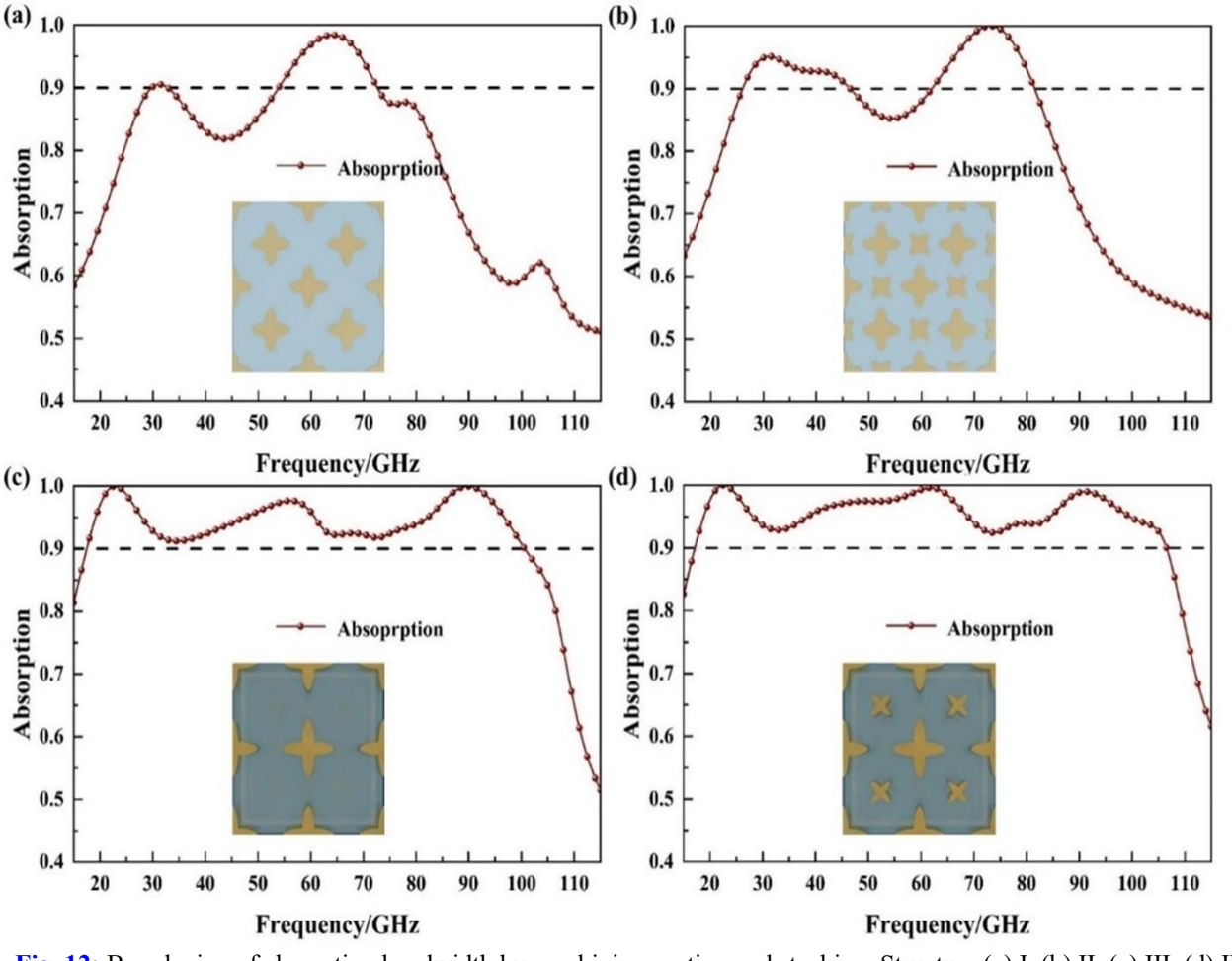

Fig. 12: Broadening of absorption bandwidth by combining nesting and stacking. Structure (a) I, (b) II, (c) III, (d) IV.

4. Conclusion

The absorber is capable of covering multiple microwave frequency bands within the range of 17.2 to 106.5 GHz and achieving an absorption efficiency of over 90%. Under the TE and TM polarizations, it can maintain excellent performance at incident angles up to 60, thereby realizing polarization insensitivity. The absorption mechanisms were analyzed through impedance-matching theory, electromagnetic field characterization (encompassing surface currents and electric fields), and an equivalent circuit model, providing a theoretical framework for broadband performance optimization. Experimentally, bow-tie reflectometry measurements closely align with simulated data, validating the design. This work offers a general approach for developing broadband flexible metamaterial absorbers, while expanding their applicability to electromagnetic shielding, smart materials, and related technological domains.

Acknowledgments

This study was supported by the National Natural Science Foundation of China (Grant No. 52175555) and the Innovative Talent Fund of the National Natural Science Foundation of China (Grant No. 62302219). In addition, this study was supported by the China Postdoctoral Science Foundation (Certificate No. 2024M763027), the Fund for Innovative Groups (No. 51821003), the Basic Research Program of Shanxi Province (2022030212120), the Basic Research Program of Shanxi Province (2022030212146), the Basic Research Program of Shanxi Province (Project no: 20210302123074) and Shanxi Provincial Science and Technology Innovation Team (202204051001011). This research work was further supported by the State Key Laboratory of Optoelectronic Dynamic Measurement Technology and Instrumentation for Extreme Environments.

Conflict of Interest

There is no conflict of interest.

Supporting Information

Not applicable.

CRediT Statement

Zeng Qu: Data curation, Data visualization, Formal analysis, Methodology, Writing, original draft. **Kangqiao Wang:** Resources, Writing, review & editing. **Qiuping Zhang:** Data curation, Validation, Writing, review & editing. **Wenhua Zhang:** Supervision, Funding acquisition, Writing, review & editing. **Yuanhao Huang:** Data visualization, Formal analysis, Writing. Yibin Gong: Data curation, Formal analysis,Writing. **Haojian Wang:** Formal analysis, Formal analysis, Writing. **Mengyuan Zhao:** Data curation, Data visualization. **Yuanhuui Wang:** Data visualization, Formal analysis. **Zhumao Lu:** Writing, original draft. **Jiayun Wang:** Supervision, Funding acquisition. **Binzhen Zhang:** Conceptualization, Supervision, Writing, review & editing.

References

[1] N. I. Landy, S. Sajuyigbe, J. J. Mock, D. R. Smith, W. J. Padilla, Perfect Metamaterial Absorber, *Physical Review Letters*, 2008, **100**, 207402, doi: 10.1103/PhysRevLett.100.207402.

[2] Y. Chen, Z. Y. Shen, H. L. Yang, Q. H. Zhang, Ultrabroadband Absorbers and Bi-Functional Sensors for Water-Based Metamaterials, *IEEE Sensors Journal*, 2024, **24**, 22307-22316, doi: 10.1109/JSEN.2024.3408226.

[3] H. L. Zhu, Y. Zhang, L. F. Ye, Y. K. Li, Z. Dang, R. M. Xu, B. Yan, A High Q-Factor Metamaterial Absorber and Its Refractive Index Sensing Characteristics, *IEEE Transactions on Microwave Theory and Techniques*, 2022, **70**, 5383-5391, doi: 10.1109/TMTT.2022.3218041.

[4] D. X. Wang, K. D. Xu, S. Y. Luo, Y. Q. Cui, L. Y. Zhang, J. L. Cui, A High Q-Factor Dual-Band Terahertz Metamaterial Absorber and Its Sensing Characteristics, *Nanoscale*, 2023, **15**, 3398-3407, doi: 10.1039/d2nr05820k.

[5] Z. Q. Ren, S. Q. Deng, J. D. Shao, Y. Y. Si, C. Zhou, J. J. Luo, T. Wang, J. Y. Li, J. X. Li, H. P. Liu, X. Qi, P. K. Wang, A. Yin, L. J. Wu, S. Z. Yu, Y. M. Zhu, J. Chen, S. Das, J. Wei, Z. H. Chen, Ultrahigh-power-density flexible piezoelectric energy harvester based on freestanding ferroelectric oxide thin films, *Nature Communications*, 2025, **16**, 3192, doi: 10.1038/s41467-025-58386-1.

[6] Z. Qu, J. F. Kang, W. Li, B. Y. Yao, H. Deng, Y. Q. Wei, H. H. Jing, X. H. Li, J. P. Duan, B. Z. Zhang, Microstructure-based high-quality factor terahertz metamaterial bio-detection sensor, *Advanced Composites and Hybrid Materials*, 2023, **6**, 100, doi: 10.1007/s42114-023-00679-4.

[7] I. Patrick, S. Adhikari, M. I. Hussein, Metaharvesting: Emergent energy harvesting by piezoelectric metamaterials, *Journal of Sound and Vibration*, 2023, **553**, 117627, doi: 10.1098/rspa.2024.0033.

[8] Y. Q. Wei, J. P. Duan, H. H. Jing, H. M. Yang, H. Deng, C. W. Song, J. Y. Wang, Z. Qu, B. Z. Zhang, Scalable, Dual-Band Metasurface Array for Electromagnetic Energy Harvesting and Wireless Power Transfer, *Micromachines*, 2022, **13**, 1712, doi: 10.3390/mi13101712.

[9] L. Li, X. M. Zhang, C. Y. Song, Y. Huang, Progress, Challenges and Perspective on Metasurfaces for Ambient Radio Frequency Energy Harvesting, *Applied Physics Letters*, 2020, **116**, 060501, doi: 10.1063/1.5140966.

[10] Y. Yao, R. Shankar, M. A. Kats, Y. Song, J. Kong, M. Loncar, F. Capasso, Electrically Tunable Metasurface Perfect Absorbers for Ultrathin Mid-Infrared Optical Modulators, *Nano Letters*, 2014, **14**, 6526 - 6532, doi: 10.1021/nl503104n.

[11] D. X. Li, X. Y. Wu, Z. W. Chen, T. Liu, X. J. Mu, Surface-enhanced spectroscopy technology based on metamaterials, *Nature Reviews Materials*, 2025, **11**, 60, doi: 10.1038/s41378-025-00905-7.

[12] N. K. Narayanaswamy, T. Y. Satheesha, Y. Alzahrani, A. Pandey, A. K. Dwivedi, V. Singh, M. Tolani, Metasurface absorber for millimeter waves: a deep learning-optimized approach for enhancing the isolation of wideband dual-port MIMO antennas, *Scientific Reports*, 2024, **14**, 30199, doi: 10.1038/s41598-024-81854-5.

[13] G. Isić, B. Vasić, D. C. Zografopoulos, R. Beccherelli, R. Gajić, Electrically Tunable Critically Coupled Terahertz Metamaterial Absorber Based on Nematic Liquid Crystals, *Physical Review Applied*, 2015, **3**, 064007, doi: 10.1103/PhysRevApplied.3.064007.

[14] F. Ding, J. Dai, Y. T. Chen, J. F. Zhu, Y. Jin, S. I. Bozhevolnyi, Broadband near-infrared metamaterial absorbers utilizing highly lossy metals, *Scientific Reports*, 2016, **6**, 39445, doi: 10.1038/srep39445.

[15] T. Li, C. Q. Bao, P. Huang, Q. He, G. F. Song, An ultra-wide-angle metasurface absorber operating in the ultraviolet to visible range, *Optics Communications*, 2024, 123456, doi: 10.1016/j.optcom.2024.130811.

[16] L. Q. Cong, S. Y. Tan, R. Yahiaoui, F. P. Yan, W. L. Zhang, R. Singh, Experimental demonstration of ultrasensitive sensing with terahertz metamaterial absorbers: A comparison with the metasurfaces, *Applied Physics Letters*, 2015, **106**, 031107, doi: 10.1063/1.4906109.

[17] L. Li, X. M. Zhang, C. Y. Song, W. Z. Zhang, T. Y. Jia, Y. Huang, Compact Dual-Band, Wide-Angle, Polarization-Angle-Independent Rectifying Metasurface for Ambient Energy Harvesting and Wireless Power Transfer, *IEEE Transactions on Microwave Theory and Techniques*, 2021, **69**(3), 1972-1986, doi: 10.1109/TMTT.2020.3040962.

[18] M. Zhang, Z. Y. Song, Switchable terahertz metamaterial absorber with broadband absorption and multiband absorption, *Optics Express*, 2021, **29**, 21551-21561, doi: 10.1364/OE.432967.

[19] D. Chen, B. J. Xu, X. J. Xue, X. G. Wang, Y. Hao, Ultra-broadband dual-square ring metamaterial absorbers from visible to far-infrared region, *Optics Communications*, 2023, **530**, 129124, doi: 10.1016/j.optcom.2022.129124.

[20] Z. Qu, H. H. Jing, H. Deng, Y. Q. Wei, J. F. Kang, X. L. Wu, B. L. Mi, R. R. Li, J. Y. Wang, J. P. Duan, Q. P. Zhang, B. Z. Zhang, Ultra-wideband electromagnetic interference suppression lightweight metamaterial absorber based on S/C/X frequency band, *Advanced Composites and Hybrid Materials*, 2023, **6**, 156, doi: 10.1007/s42114-023-00734-0.

[21] D. D. Chen, B. J. Xu, X. J. Xue, X. G. Wang, Y. Hao, Ultra-broadband dual-square ring metamaterial absorbers from visible to far-infrared region, *Optics Communications*, 2023, **530**, doi: 10.1016/j.optcom.2022.129124.

[22] M. H. Luo, S. Shen, L. Zhou, S. L. Wu, Y. Zhou, L. S. Chen, Broadband, wide-angle, and polarization-independent metamaterial absorber for the visible regime, *Optics Express*, 2017, **25**, 16715-16724, doi: 10.1364/OE.25.016715.

[23] Z. Qu, J. X. Hao, H. H. Jing, Y. Q. Wei, J. P. Duan, J. Y. Wang, B. Z. Zhang, An ultra-thin ultra-broadband microwave absorber for radar stealth, *Advanced Composites and Hybrid Materials*, 2022, **5**, 1778-1785, doi: 10.1007/s42114-022-00429-y.

[24] J. Xu, Y. C. Fan, X. P. Su, J. Guo, J. X. Zhu, Q. H. Fu, F. L. Zhang, Broadband and wide angle microwave absorption with optically transparent metamaterial, *Optical Materials*, 2021, **113**, 110852, doi: 10.1016/j.optmat.2021.110852.

[25] H. H. Jing, J. P. Duan, Y. Q. Wei, J. X. Hao, Z. Qu, J. Y. Wang, B. Z. Zhang, An ultra-broadband flexible polarization-insensitive microwave metamaterial absorber, *Materials Research Express*, 2022, **9**, 025802. doi: 10.1088/2053-1591/ac5484.

[26] C. Yang, H. C. Chang, L. Xiao, Y. C. Qu, Visible and NIR transparent broadband microwave absorption metamaterial based on silver nanowires, *Optical Materials*, 2022, **131**, 112464. doi: 10.1016/j.optmat.2022.112464.

[27] M. Manzoor, X. Kexin, L. Han, C. Ruan, Polarization and Angle Insensitive Ultrathin Wideband Metamaterial Absorber based on Indium-Tin-Oxide, *Cross Straight Radio Science and Wireless Technology Conference* (CSRSWTC), 2024. doi: 10.1109/CSRSWTC64338.2024.10811522.

[28] N. K. Narayanaswamy, T. Y. Satheesha, Y. Alzahrani, A. Pandey, A. K. Dwivedi, V. Singh, M. Tolani, Meta surface absorber for millimeter waves: a deep learning-optimized approach for enhancing the isolation of wideband dual-port MIMO antennas, *Scientific Reports*, 2024, **14**, 30199. doi: 10.1038/s41598-024-81854-5.

[29] A. Teber, FR2/mmWave, N258 and N261 Bands, 5G Frequency-Compatible Ultra-Thin Metamaterial Absorber with Polarization Insensitivity for EMI shielding Applications, *Advanced Theory and Simulations*, 2024, **7**, 2400332. doi: 10.1002/adts.202400332.

[30] D. R. Smith, D. C. Vier, Th. Koschny, C. M. Soukoulis, Electromagnetic parameter retrieval from inhomogeneous metamaterials, *Physical Review E*, 2005, **71**, 036617, doi: 10.1103/PhysRevE.71.036617.

[31] X. K. Kong, S. L. Jiang, L. Q. Kong, Q. Wang, H. B. Hu, X. Zhang, X. Zhao, Transparent metamaterial absorber with broadband radar cross-section (RCS) reduction for solar arrays, IET Microwaves, *Antennas & Propagation*, 2020, **14**, 1580-1586, doi: 10.1049/iet-map.2020.0369.

[32] Y. Q. Zhang, X. H. Deng, J. Q. Geng, Z. P. Xiong, P. Hu, Terahertz ultra-wideband metamaterial absorber based on

superposition optimization, *Materials Research Bulletin*, 2025, **192**, 113589. doi: 10.1016/j.materresbull.2025.113589.

[33] B. X. Wang, L. L. Wang, G. Z. Wang, W. Q. Huang, X. F. Li, X. Zhai, Theoretical Investigation of Broadband and Wide-Angle Terahertz Metamaterial Absorber, *IEEE Photonics Technology Letters*, 2013, **25**, 114-117, doi: 10.1109/LPT.2013.2289299.